Anisotropy links cell shapes to tissue flow during convergent extension

Xun Wang[a,1], Matthias Merkel[b,c,d,1], Leo B. Sutter[b,c,1], Gonca Erdemci-Tandogan[b,c,2], M. Lisa Manning[b,c], and Karen E. Kasza[a,3]

[a]Department of Mechanical Engineering, Columbia University, New York, NY 10027; [b]Department of Physics, Syracuse University, Syracuse, NY 13244; [c]BioInspired Institute, Syracuse University, Syracuse, NY 13244; and [d]Centre de Physique Théorique (CPT), Turing Center for Living Systems, Aix Marseille Univ, Université de Toulon, CNRS, 13009 Marseille, France

Edited by Stanislav Y. Shvartsman, Princeton University, Princeton, NJ, and accepted by Editorial Board Member Allan C. Spradling March 30, 2020 (received for review September 24, 2019)

Within developing embryos, tissues flow and reorganize dramatically on timescales as short as minutes. This includes epithelial tissues, which often narrow and elongate in convergent extension movements due to anisotropies in external forces or in internal cell-generated forces. However, the mechanisms that allow or prevent tissue reorganization, especially in the presence of strongly anisotropic forces, remain unclear. We study this question in the converging and extending *Drosophila* germband epithelium, which displays planar-polarized myosin II and experiences anisotropic forces from neighboring tissues. We show that, in contrast to isotropic tissues, cell shape alone is not sufficient to predict the onset of rapid cell rearrangement. From theoretical considerations and vertex model simulations, we predict that in anisotropic tissues, two experimentally accessible metrics of cell patterns—the cell shape index and a cell alignment index—are required to determine whether an anisotropic tissue is in a solid-like or fluid-like state. We show that changes in cell shape and alignment over time in the *Drosophila* germband predict the onset of rapid cell rearrangement in both wild-type and *snail twist* mutant embryos, where our theoretical prediction is further improved when we also account for cell packing disorder. These findings suggest that convergent extension is associated with a transition to more fluid-like tissue behavior, which may help accommodate tissue-shape changes during rapid developmental events.

epithelia | morphogenesis | vertex models | *Drosophila*

The ability of tissues to physically change shape and move is essential to fundamental morphogenetic processes that produce the diverse shapes and structures of tissues in multicellular organisms during development (1, 2). Developing tissues are composed of cells that can dynamically change their behavior and actively generate forces to influence tissue reorganization and movement (3–8). Remarkably, tissues dramatically deform and flow on timescales as short as minutes or as long as days (6). Recent studies highlight that tissue movements within developing embryos can be linked with the tissue fluidity (8–11), and computational models assuming predominantly fluid-like tissue behavior predict aspects of tissue movements (12, 13). Fluid-like tissues accommodate tissue flow and remodeling, while solid-like tissues resist flow. Yet, the mechanisms underlying the mechanical behavior of developing tissues remain poorly understood, in part due to the challenges of sophisticated mechanical measurements inside embryos and the lack of unifying theoretical frameworks for the mechanics of multicellular tissues (6, 7, 14).

Epithelial tissue sheets play pivotal roles in physically shaping the embryos of many organisms (2), often through convergent extension movements that narrow and elongate tissues. Convergent extension is highly conserved and used in elongating tissues, tubular organs, and overall body shapes (15). Convergent-extension movements require anisotropies in either external forces that deform the tissue or asymmetries in cell behaviors that internally drive tissue-shape change. Indeed, an essential feature of many epithelia in vivo is anisotropy in the plane of the tissue sheet, a property known as *planar polarity*, which is associated with the asymmetric localization of key molecules inside cells (16–19). For example, during *Drosophila* body axis elongation, the force-generating motor protein myosin II is specifically enriched at cell edges in the epithelial germband tissue that are oriented perpendicular to the head-to-tail body axis (20, 21) (Fig. 1*A*). Planar-polarized myosin is required for cell rearrangements that converge and extend the tissue to rapidly elongate the body and is thought to produce anisotropic tensions in the tissue (12, 13, 21–25). In addition, the *Drosophila* germband experiences external forces from neighboring tissues, including the mesoderm and endoderm, which have been linked to cell-shape changes in the germband during convergent extension (26–29) (Fig. 1*A*). Despite being fundamental to epithelial tissue behavior in vivo, it is unclear how such anisotropies arising from internal myosin planar polarity and external forces influence epithelial-tissue mechanical behavior, particularly whether the tissue behaves more like a fluid or a solid.

Vertex models have proven a useful framework for theoretically studying the mechanical behavior of confluent epithelial

Significance

Cells and tissues dramatically change shape to form functional tissues and organs during embryonic development. It is not well understood how mechanical and biological factors influence whether a developing tissue flows like a fluid or instead resists shape changes like a solid. Combining experimental studies in the fruit fly embryo with modeling approaches, we show that the shapes and alignment of cells within tissues can help to elucidate and predict how tissues change shape during development and how defects in these processes can result in abnormalities in embryo shape. Because many genes and cell behaviors are shared between fruit flies and humans, these results may reveal fundamental mechanisms underlying human development.

Author contributions: X.W., M.M., M.L.M., and K.E.K. designed research; X.W., M.M., L.B.S., and G.E.-T. performed research; X.W., M.M., G.E.-T., M.L.M., and K.E.K. analyzed data; and X.W., M.M., M.L.M., and K.E.K. wrote the paper.

The authors declare no competing interest.

This article is a PNAS Direct Submission. S.Y.S. is a guest editor invited by the Editorial Board.

Published under the PNAS license.

Data deposition: The custom code used in this study to extract the average triangle-based *Q* tensor from images segmented using SEGGA is available at https://github.com/mmerkel/triangles-segga.

[1] X.W., M.M., and L.B.S. contributed equally to this work.

[2] Present address: Institute of Biomaterials and Biomedical Engineering, University of Toronto, Toronto, ON, Canada M5S 3G9.

[3] To whom correspondence may be addressed. Email: karen.kasza@columbia.edu.

This article contains supporting information online at https://www.pnas.org/lookup/suppl/doi:10.1073/pnas.1916418117/-/DCSupplemental.

First published May 28, 2020.

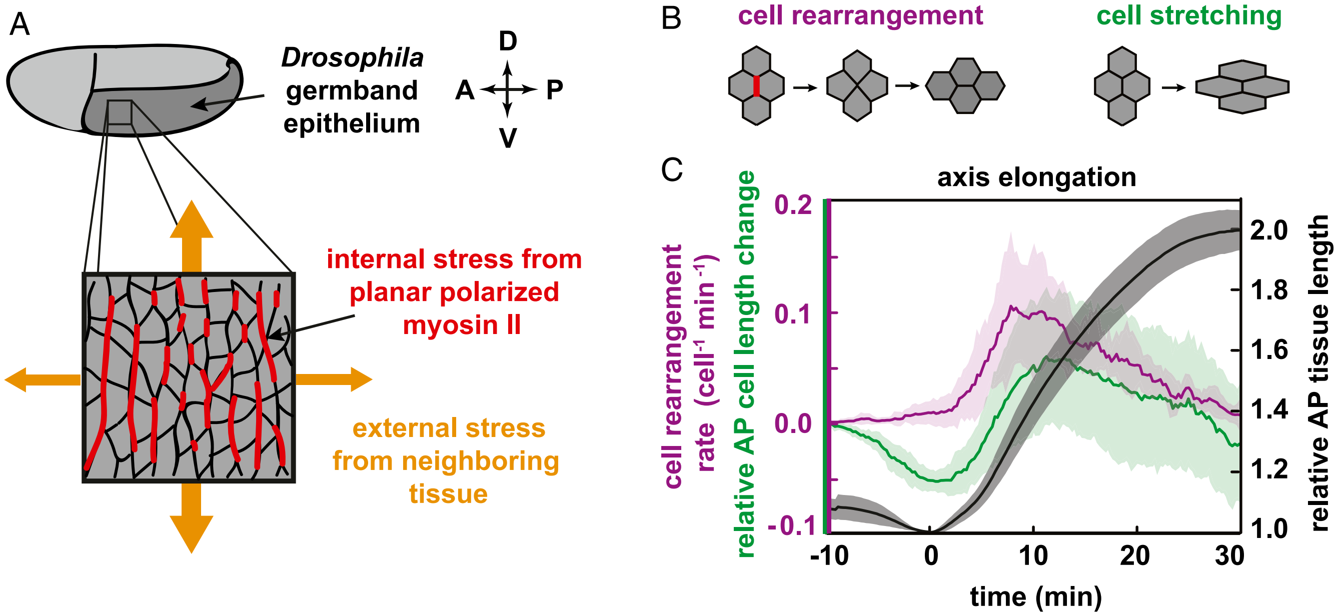

Fig. 1. Cell shapes and cell rearrangements in the converging and extending *Drosophila* germband epithelium during axis elongation. (*A*) Schematic of *Drosophila* body axis elongation. The germband epithelium (dark gray) narrows and elongates along the head-to-tail body axis in a convergent extension movement. The tissue is anisotropic, experiencing internal stresses from planar-polarized patterns of myosin II (red) within the tissue as well as external stresses (orange) due to the movements of neighboring tissue. (*B*) Schematic of oriented cell rearrangement and cell-shape change. (*C*) The germband epithelium doubles in length along the head-to-tail AP axis in 30 min (black). Cell rearrangements are thought to drive tissue elongation (magenta), and cell-shape changes also contribute (green). Tissue elongation begins at $t = 0$. The cell rearrangement rate includes cell-neighbor changes through T1 processes and higher-order rosette rearrangements. Relative cell length along the AP axis is normalized by the value at $t = -10$ min. Mean and SD between embryos is plotted ($n = 8$ embryos with an average of 306 cells analyzed per embryo per time point).

tissues (30, 31), including the packings of cells in tissues (32–34) and the dynamics of remodeling tissues (23, 32, 35–37). Recent studies of the energy barriers to cell rearrangement in isotropic vertex models, which assume no anisotropy in either internal tensions at cell–cell contacts or in external forces, have revealed a transition from solid to fluid behavior, which depends on whether large or small contacts are favored between neighboring cells. The transition is indicated by a single parameter describing cell shape, $\bar{p}$, which is the average value in the tissue of cell perimeter divided by the square root of cell area (38–40). When cells prefer smaller contacts with neighbors, $\bar{p}$ is small, and the tissue is solid-like. Above a critical value of $\bar{p} = p_o^*$, the tissue becomes fluid-like. The isotropic vertex model successfully predicts that cell shapes identify the transition from fluid-like to solid-like behavior in cultured primary bronchial epithelial tissues; initial modeling work suggested that the critical cell shape p_o^* is close to 3.81 (39), in good agreement with the experiments (41). Such a simple way to infer tissue behavior from static images is appealing, particularly for tissues that are inaccessible to mechanical measurements or live imaging.

However, subsequent work has shown that the precise value of p_o^* depends on specific features of the cell packing, such as the number of manyfold coordinated vertices (42) or the distribution of neighbor numbers in the packing (43–45), though the latter feature has never been studied systematically. In addition, these previous vertex model studies did not account for effects of anisotropy, potentially limiting their use in the study of converging and extending tissues.

Here, we combine confocal imaging and quantitative image analysis with a vertex model of anisotropic tissues to study epithelial convergent extension during *Drosophila* body axis elongation. We show that cell shape alone is not sufficient to predict the onset of rapid cell rearrangement during convergent extension in the *Drosophila* germband, which exhibits anisotropies arising from internal forces from planar-polarized myosin and external forces from neighboring tissue movements. Instead, we show that, for anisotropic tissues, such as the *Drosophila* germband, anisotropy shifts the predicted transition between solid-like and fluid-like behavior and so must be taken into account, which can be achieved by considering both cell shape and cell alignment in the tissue. We find that the onset of cell rearrangement and tissue flow during convergent extension in wild-type and mutant *Drosophila* embryos is more accurately described by a combination of cell shape and alignment than by cell shape alone. Moreover, we use experimentally accessible features of cell-neighbor relationships to quantify cell packing disorder and pinpoint p_o^*, which further improves our predictions. These findings suggest that convergent extension is associated with a transition from solid-like to more fluid-like tissue behavior, which may help to accommodate dramatic epithelial tissue-shape changes during rapid axis elongation.

Results

Cell Shape Alone Is Not Sufficient to Predict the Onset of Rapid Cell Rearrangement in the *Drosophila* Germband Epithelium.

To explore the mechanical behavior of a converging and extending epithelial tissue in vivo, we investigated the *Drosophila* germband, a well-studied tissue that has internal anisotropies arising from planar-polarized myosin (20–25, 46) and also experiences external forces from neighboring developmental processes that stretch the tissue (26, 27). The germband rapidly extends along the anterior–posterior (AP) axis while narrowing along the dorsal–ventral (DV) axis (Fig. 1*A*), roughly doubling the length of the head-to-tail body axis in just 30 min (47) (Fig. 1*C*). Convergent extension in the *Drosophila* germband is driven by a combination of cell rearrangements and cell-shape changes (Fig. 1 *B* and *C*). The dominant contribution is from cell rearrangement (21, 22, 28, 47), which requires a planar-polarized pattern of myosin localization across the tissue (20, 21) that is thought to be the driving force for rearrangement (21, 23, 24, 46). Cell stretching along the AP axis also contributes to tissue elongation and coincides with movements of neighboring tissues (26–28, 48, 49), indicating that external forces play an important role in tissue behavior. Despite significant study of this tissue, a comprehensive framework for understanding its mechanical behavior is lacking, in part because direct mechanical measurements inside the *Drosophila* embryo, and more generally for epithelial tissues in vivo, continue to be a challenge (50–52).

To gain insight into the origins of mechanical behavior in the *Drosophila* germband epithelium, we first tested the theoretical prediction of the vertex model that cell shapes can be linked to tissue mechanics. In the isotropic vertex model, tissue mechanical behavior is reflected in a single parameter, the average cell shape index $\bar{p}$ (38–41). To quantify cell shapes in the *Drosophila* germband, we used confocal time-lapse imaging of embryos with fluorescently tagged cell membranes (53) and segmented the resulting time-lapse movies (28) (Fig. 2*A* and *SI Appendix*, Fig. S1). Prior to the onset of tissue elongation, individual cells take on roughly isotropic shapes and become more elongated over time (Fig. 2 *A* and *B*), consistent with previous observations (26–28, 54). Ten minutes prior to tissue elongation, the cell shape index $\bar{p}$ averaged over eight wild-type embryos was just above 3.81. Eight minutes before the onset of tissue elongation, $\bar{p}$ started to increase before reaching a steady value of 3.98 about 20 min after the onset of tissue elongation (Fig. 2*B*). The average cell shape index prior to tissue elongation, $\bar{p} = 3.81$ (dashed line, Fig. 2*B*), was close to the value associated with isotropic solid-like tissues in previous work (38–40), suggesting that the tissue may be solid-like prior to elongation.

We next asked how these cell shapes vary among the individual embryos and correlate with tissue mechanical behavior. As an experimentally accessible read-out of tissue fluidity, we used the instantaneous rate of cell rearrangements occurring within the germband tissue (Fig. 1*C*), where higher rearrangement rates were associated with more fluid-like behavior and/or larger driving forces. Plotting instantaneous cell rearrangment rate versus $\bar{p}$ at each time point from movies of individual wild-type *Drosophila* embryos, we found that the onset of rapid cell rearrangement occurred at different values of $\bar{p}$ for each embryo, ranging from 3.83 to 3.90 for a cutoff rearrangement rate per cell

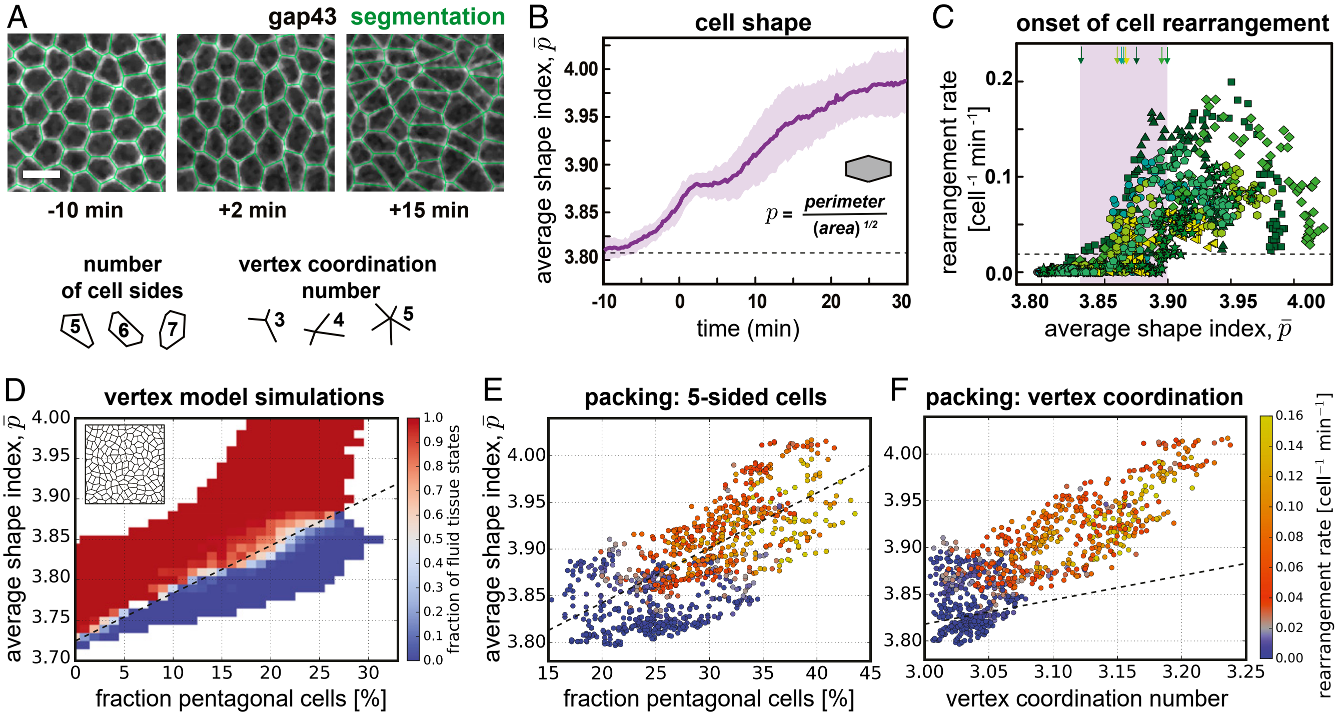

Fig. 2. Cell shape and packing disorder alone are not sufficient to predict the onset of cell rearrangements in the *Drosophila* germband. (*A*) Confocal images from time-lapse movies of epithelial cell patterns in the ventrolateral region of the germband tissue during *Drosophila* axis elongation. Cell outlines were visualized by using the fluorescently tagged cell membrane marker gap43:mCherry (53). Anterior left, ventral down. Images with overlaid polygon representations used to quantify cell shapes (green) are shown. (Scale bar, 10 μm.) See *SI Appendix*, Fig. S1. (*B*) The average cell shape index $\bar{p}$ in the germband before and during convergent extension. The cell shape index, p, is calculated for each cell from the ratio of cell perimeter to square root of cell area, and the average value for cells in the tissue, $\bar{p}$, is calculated at each time point. The mean and SD between embryos is plotted. Dashed line denotes the reported value for the solid–fluid transition in the isotropic vertex model, $\bar{p} = 3.81$. See also *SI Appendix*, Fig. S2. (*C*) The instantaneous rate of cell rearrangements per cell versus the average cell shape index $\bar{p}$ from movies of individual embryos at time points before and during convergent extension in eight wild-type embryos (different symbols correspond to different embryos). Small green arrows indicate the values of $\bar{p}$ at the onset of rapid cell rearrangement (>0.02 per cell per min; dashed line) in different embryos. The shaded region denotes values of $\bar{p}$ for which different embryos display distinct behaviors, either showing rapid cell rearrangement or not. Thus, a fixed value of $\bar{p}$ is not sufficient to determine the onset of rearrangement. (*D*) In vertex model simulations, the solid–fluid transition depends on exactly how cells are packed in the tissue (*SI Appendix*, *Materials and Methods* and Fig. S3). In model tissues, we find a linear dependence of the critical cell shape index on the fraction of pentagonal cells f_5, which is a metric for packing disorder. The dashed line represents a linear fit to this transition: $p_o^* = 3.725 + 0.59 f_5$. (*E*) The relationship between $\bar{p}$ and f_5 for eight wild-type embryos, with each point representing a time point in a single embryo. The dashed line is the prediction from vertex model results (same as in *D*). (*F*) The relationship between $\bar{p}$ and vertex coordination number for eight wild-type embryos, with each point representing a time point in a single embryo. The dashed line is the prediction from ref. 42. (*E* and *F*) Instantaneous cell rearrangment rate per cell in the tissue is represented by the color of each point, with blue indicating low rearrangement rates and red to yellow indicating high rearrangement rates.

of 0.02 min^{-1} (Fig. 2*C*). We verified that we observed a similar variation in the values of $\bar{p}$ for different cutoff values (*SI Appendix*, Fig. S2). This suggests that, in the germband epithelium, comparing the cell shape index $\bar{p}$ to a fixed critical value (e.g., 3.81) is not sufficient to predict tissue behavior.

Cellular Packing Disorder Is Not Sufficient to Predict the Onset of Rapid Cell Rearrangement in the Germband. Recent vertex model simulations suggest that $\bar{p} = 3.81$ is often insufficient to separate solid from fluid tissue behavior, as the precise location of the solid–fluid transition depends on how exactly cells are packed in the tissue (42–45). A hexagonal packing has no packing disorder, while each cell with neighbor number different from six increases the packing disorder in the tissue. In the modeling literature, this disorder is typically generated either by allowing manyfold coordinated vertices (i.e., vertices at which more than three cells meet) or using simulation preparation protocols that create cell-neighbor numbers other than six. Including manyfold vertices in simulations is natural, as they are observed in the germband epithelium (54) and are often formed during cell rearrangements involving four or more cells (21, 22). Moreover, recent theoretical work has predicted how the presence of manyfold vertices increases the critical shape index (42).

We wondered whether cell packing disorder quantified by the vertex coordination number z could explain the observed embryo-to-embryo variability in $\bar{p}$ at the transition point in wild-type embryos (Fig. 2*C* and *SI Appendix*, Fig. S2). To test this idea, we plotted $\bar{p}$ versus z at each time point and color-coded the data based on the instantaneous cell rearrangement rate, pooling the data from all wild-type embryos (Fig. 2*F*). To isolate the changes in mechanical behavior of the germband during convergent extension from later developmental events, we focused on times $t \leq 20$ min after the onset of tissue elongation, well before cell divisions begin in the germband. If vertex coordination were sufficient to explain the germband behavior, then the theoretically determined line (dashed line) should separate regions with a low cell rearrangement rate (blue symbols) from regions with a high cell rearrangement rate (red, orange, and yellow symbols) (Fig. 2*F*). However, this was not the case, indicating that the prediction from ref. 42. alone is not sufficient to account for the germband behavior during this stage.

Next, we asked if other aspects of packing disorder could affect tissue fluidity. Even without manyfold vertices, it is possible to generate packings in silico with differences in packing disorder just by altering the preparation protocol. Since this has not been systematically studied, we performed a large number of vertex model simulations where we varied the packing disorder (*SI Appendix*, Fig. S3 *A* and *B*). In our simulations, the transition point was well predicted by the fraction of pentagonal cells, i.e., cells that have exactly five neighbors, with a linear dependence (Fig. 2*D* and *SI Appendix*, Fig. S3 *C* and *D*). In particular, without any pentagonal cells, we recovered the predicted transition point of ≈3.72 for tissues consisting only of hexagonal cells (33, 38). In comparison, the reported value of 3.81 corresponded to a fraction of ≈15% pentagonal cells (Fig. 2*D*). While additional aspects of cell packing likely affect the transition, these results suggest that the fraction of pentagonal cells may also be a good predictor for the transition point in isotropic tissues.

To test whether this second measure of packing disorder could explain the variability in $\bar{p}$ at the transition in wild-type embryos, we plotted $\bar{p}$ versus the fraction of pentagonal cells at each time point, again color-coding the data based on the instantaneous cell rearrangement rate and pooling data from all wild-type embryos (Fig. 2*E* and *SI Appendix*, Fig. S2). We found that the packing disorder quantified by the fraction of pentagonal cells was also insufficient to explain the onset of cell rearrangements.

Our results suggest that two measures of packing disorder, the vertex coordination number and fraction of pentagonal cells, have at least partially independent effects on the isotropic vertex model transition point. However, neither of them is sufficient to understand the transition to high cell rearrangement rates in the *Drosophila* germband.

Theoretical Considerations and Vertex Model Simulations Predict a Shift of the Solid–Fluid Transition in Anisotropic Tissues. To study whether anisotropies in the germband could affect the relation between the cell shape index and cell rearrangement rate, we used vertex model simulations to test how tissue anisotropy, introduced into the model in different ways, affects tissue fluidity.

First, we introduced anisotropy by applying an external deformation, mimicking the effects of forces exerted by neighboring morphogenetic processes, and then studied force-balanced states of the model tissue (Fig. 3*A*). As a metric for tissue stiffness, we measured the shear modulus of the model tissue, which describes with how much force a tissue resists changes in shape. A vanishing shear modulus corresponds to fluid behavior, where the tissue flows and cells rearrange in response to any driving force, whereas a positive shear modulus indicates solid behavior, where the tissue does not flow so long as the driving force is not too large. We then analyzed how the shear modulus correlates with $\bar{p}$ for different amounts of global tissue deformation, quantified by the strain ε (Fig. 3*B*). For small strain, we recovered the behavior of the isotropic vertex model. The shear modulus was finite when $\bar{p}$ was small and vanished above a critical cell shape index, which was $p_o^* = 3.94$ for our simulations (Fig. 3*B*, blue symbols). For larger strains, we found that the critical value of the shape index at the transition between solid-like and fluid-like behavior generally increased with the amount of strain (Fig. 3*B*). Indeed, $\bar{p}$ for cells in a deformed, solid tissue can be higher than for cells in an undeformed, fluid tissue. This suggests that anisotropy affects the critical shape index at which the tissue transitions between solid and fluid behavior.

Some of us recently developed a theoretical understanding for a shift in the critical shape index when deforming a vertex model tissue (45). In the limit of small deformations by some strain ε and without cell rearrangements, the critical value of $\bar{p}$ increases from p_o^* to $p_o^* + b\varepsilon^2$, where b is a constant prefactor. To compare this formula to the vertex model simulations (Fig. 3 *A* and *B*), we need to take into account that cell rearrangements occur in our simulations. Removing their contribution from the overall tissue strain ε left us with a parameter Q (Fig. 3*C*) (*SI Appendix*, *SI Materials and Methods*), which can be quantified using a triangulation of the tissue created from the positions of cell centers (*SI Appendix*, *SI Materials and Methods*) (55, 56). We term Q a "shape alignment index," as Q is nonzero only when the long axes of cells are aligned. We emphasize that, unlike the nematic-order parameter for liquid crystals, the cell alignment parameter Q is additionally modulated by the degree of cell shape anisotropy; tissues with the same degree of cell alignment but more elongated cells have a higher Q (Fig. 3*C*). In other words, Q can be regarded as a measure for tissue anisotropy. After accounting for cell rearrangements, we expect the transition point in anisotropic tissues to shift from the isotropic value p_o^* to (*SI Appendix*, *SI Materials and Methods*):

$$\bar{p}_{crit} = p_o^* + 4bQ^2. \qquad [1]$$

Indeed, comparing this equation to vertex model simulations yields a good fit with the simulation results (Fig. 3*D*, solid line), with fit parameters $p_o^* = 3.94$ and $b = 0.43$ (*SI Appendix*, Fig. S4). We confirmed that cell-area variation did not significantly affect these findings (*SI Appendix*, Fig. S5). In principle, we expect both the transition point p_o^* and the precise value of b to depend on the packing disorder, but our best-fit value for b was consistent with published results (45). Therefore, we used $b = 0.43$ for the

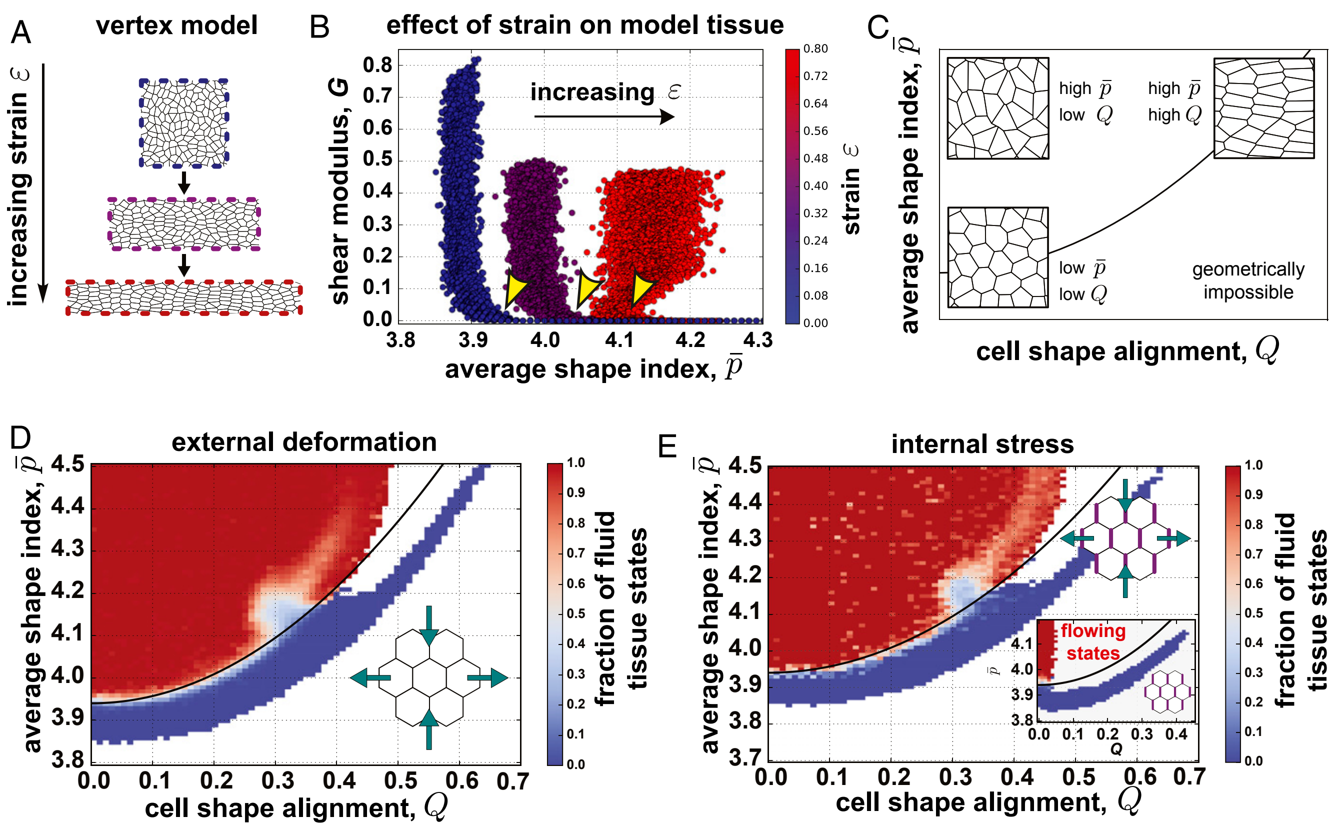

Fig. 3. The solid-to-fluid transition in a vertex model of anisotropic tissues. (*A*) We study the effect of anisotropies on the solid–fluid transition in the vertex model by externally applying an anisotropic strain ε. An initially quadratic periodic box with dimensions $L_0 \times L_0$ is deformed into a box with dimensions $e^{\varepsilon}L_0 \times e^{-\varepsilon}L_0$. (*B*) Vertex model tissue rigidity as a function of the average cell shape index with different levels of externally applied strain ε (values for ε, increasing from blue to red: 0, 0.4, and 0.8). For comparison, the strain in the wild-type germband between the times $t = 0$ min and $t = 20$ min is $\varepsilon \sim 0.6$. For every force-balanced configuration, the shear modulus was analytically computed as described in *SI Appendix, SI Materials and Methods*. For zero strain, we find a transition at an average cell shape index of $\bar{p} = 3.94$ from solid behavior to fluid behavior. For increasing strain, the transition from solid to fluid behavior (i.e., the shear modulus becomes zero for a given strain) occurs at higher $\bar{p}$ (approximate positions marked by yellow arrows). Thus, a single critical cell shape index is not sufficient to determine the solid–fluid transition in an anisotropic tissue. (*C*) Cell shape and cell shape alignment can be used to characterize cell patterns in anisotropic tissues. Cell shape alignment Q characterizes both cell shape anisotropy and cell shape alignment across the tissue. While a high cell shape index $\bar{p}$ correlates with anisotropic cell shapes, the cell shape alignment Q is only high if these cells are also aligned. Conversely, low $\bar{p}$ implies low cell shape anisotropy and, thus, low Q. (*D* and *E*) Vertex model simulations for the case of an anisotropic tissue arising due to externally induced deformation (*D*) (cf. *A* and *B*), due to internal active stresses generated by an anisotropic cell–cell interfacial tension combined with externally applied deformation (*E*), and due to internal active stresses without any externally applied force (*E*, *Inset*) (*SI Appendix*). The fraction of tissue configurations that are fluid is plotted as a function of $\bar{p}$ and Q. For both internal and external sources of anisotropy, the critical shape index $\bar{p}$ marking the transition between solid states (blue) and fluid states (red) is predicted to depend quadratically on Q. White regions denote combinations of $\bar{p}$ and Q for which we did not find force-balanced states. In particular, in the case of finite tension anisotropy, we did not find any stable force-balanced fluid states, and the red fluid states in *E* all correspond to the limiting value of zero-tension anisotropy. In *SI Appendix, Materials and Methods*, we explain how the lack of fluid states for finite tension anisotropy can be explained analytically. Our findings quite generally suggest that stationary states of fluid tissues with an anisotropic cell–cell interfacial tension are difficult to stabilize even when preventing overall oriented tissue flow via the boundaries. In *D*, the solid line shows a fit of the transition to Eq. **1** with $p_o^* = 3.94$ and $b = 0.43$; *E* and *E*, *Inset* show this same line. In *D*, a deviation from Eq. **1** is only seen around $\bar{p} \sim 4.15$ and $Q \sim 0.3$, where we observe an abundance of solid states, which is likely due to the occurrence of manyfold vertices in this regime (*SI Appendix*, Fig. S4), which are known to rigidify vertex model tissue (42).

remainder of this study. Hence, for external deformation, the solid–fluid transition point in the vertex model increases quadratically with tissue anisotropy Q.

We also tested how the model predictions change when we introduce anisotropy generated by internal forces into the vertex model. We modeled myosin planar polarity as increased tensions on "vertical" cell–cell contacts (Fig. 3*E* and *SI Appendix*, Fig. S6) (23) and focused again on stationary, force-balanced states. We investigated simulations of model tissues with internal forces, both with (Fig. 3*E*) and without (Fig. 3 *E*, *Inset*) externally applied deformation. We found that in both cases, solid states exist for larger cell shape indices than the isotropic $p_o^* = 3.94$, and our results were again consistent with the fit from Fig. 3*D* (solid lines in Fig. 3*E* and Fig. 3 *E*, *Inset*). With finite anisotropic internal tensions only, we obtained states in the fluid regime that do not reach a force-balanced state (see detailed discussion in *SI Appendix*), and this explains the white region devoid of stable states in the upper middle region of Fig. 3 *E*, *Inset*. Taken together, these findings demonstrate that a combination of cell shape $\bar{p}$ and cell shape alignment Q in the vertex model indicates whether an anisotropic tissue is in a solid-like or fluid-like state, regardless of the underlying origin of anisotropy.

Cell Shape and Cell Shape Alignment Together Indicate the Onset of Cell Rearrangement during *Drosophila* Axis Elongation. We returned to our experiments to test whether a combination of $\bar{p}$ and Q would be a better predictor for the behavior of the *Drosophila* germband during convergent extension. We quantified alignment Q using the triangle method (Fig. 4*A*) and found that, prior to the onset of tissue elongation, which begins at $t = 0$ min, alignment is not very high (Fig. 4*B*). Q began to increase just prior to elongation, peaking at $t = 1$ min (Fig. 4*B* and *SI Appendix*, Fig. S7), which is consistent with observations using other cell-pattern metrics (23, 26, 28, 29). This peak in Q corresponds to stretching of cells along the DV axis, perpendicular to the axis of germband extension, and coincides with the time period during which the presumptive mesoderm is invaginating (29, 53). Q relaxes back to low levels during axis elongation (Fig. 4*B*). Plotting $\bar{p}$ versus Q at each time point from movies of individual wild-type embryos revealed common features, despite embryo-to-embryo variability (Fig. 4 *C*, *Inset*). Initially, we saw a concomitant increase of $\bar{p}$ and Q prior to the onset of convergent extension. Above $\bar{p} = 3.87$, Q decreased drastically as $\bar{p}$ continued to increase, indicating that further increases in $\bar{p}$ are associated with randomly oriented cell shapes (cf. Fig. 3*C*). Thus, cell shapes in the germband are transiently aligned around the onset of convergent extension.

We next asked whether this temporary increase in alignment could help resolve the seeming contradiction between the measured

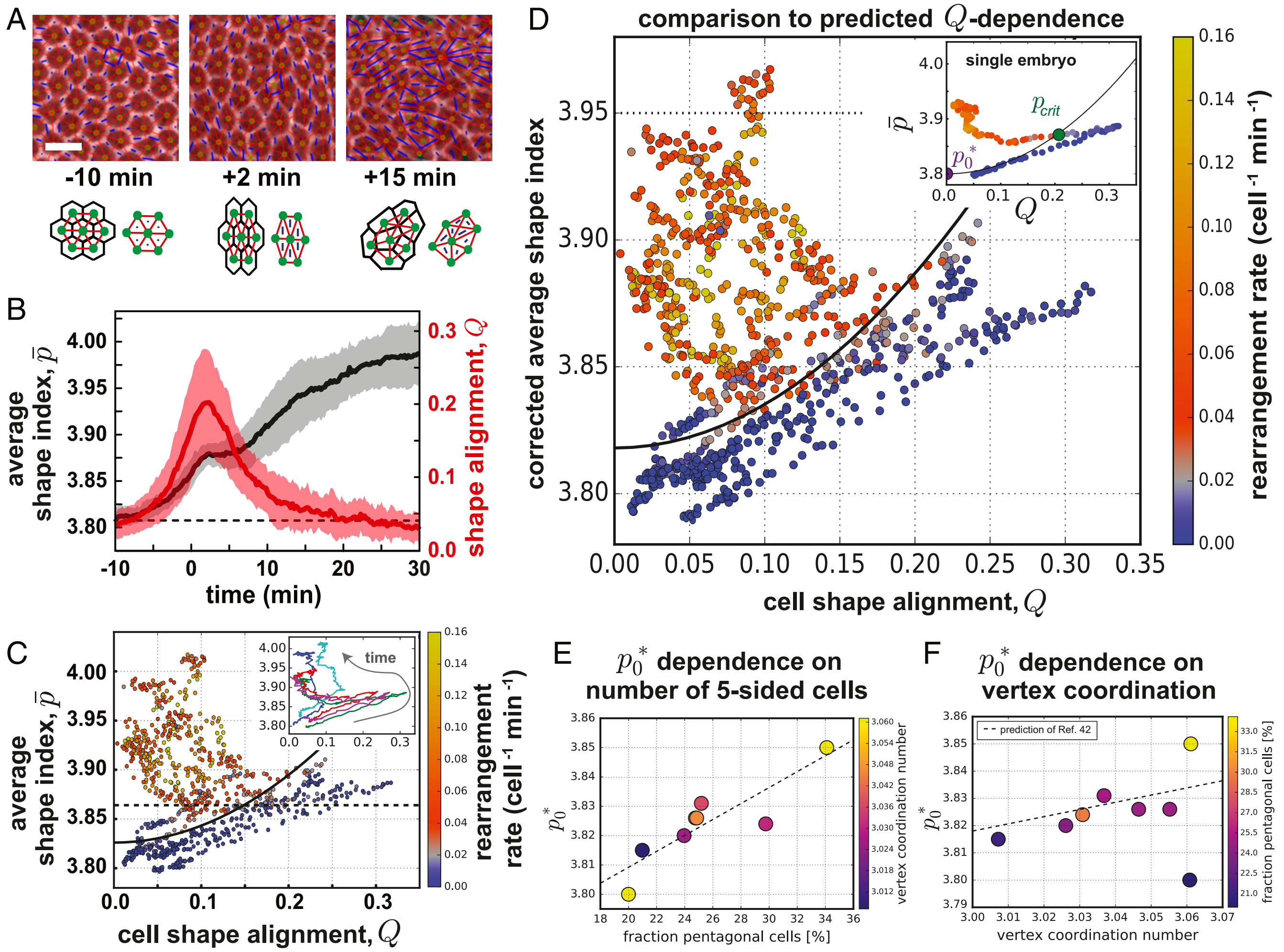

Fig. 4. Cell shape and cell shape alignment together predict the onset of cell rearrangements during *Drosophila* convergent extension. (*A*) Confocal images from time-lapse movies of epithelial cell patterns in the ventrolateral region of the germband during *Drosophila* axis elongation. Cell outlines were visualized with gap43:mCherry (53). Anterior left, ventral down. (Scale bar, 10 μm.) Images of cells with overlaid triangles that were used to quantify cell shape anisotropy. Cell centers (green dots) are connected with each other by a triangular network (red bonds). Cell shape stretches are represented by triangle stretches (blue bars), and the average cell elongation, Q, is measured (56). (*B*) The cell shape alignment index Q (red) and average cell shape index $\bar{p}$ (black, same as Fig. 2*B*) for the germband tissue before and during axis elongation. Q was calculated for each time point, and the mean and SD between embryos is plotted ($n = 8$ embryos with an average of 306 cells analyzed per embryo per time point). The onset of tissue elongation occurs at $t = 0$. The dashed line denotes the reported value for the solid–fluid transition in the isotropic vertex model, $\bar{p} = 3.81$ (39). (*C*) The relationship between $\bar{p}$ and Q for eight individual wild-type embryos, with each point representing $\bar{p}$ and Q for a time point in a single embryo. Instantaneous cell rearrangement rate per cell in the tissue is represented by the color of each point, with blue indicating low rearrangement rates and red to yellow indicating high rearrangement rates. The black solid line indicates a fit to Eq. **1** with a rearrangement-rate cutoff of 0.02 min^{-1} per cell (*SI Appendix, Materials and Methods*), from which we extract $p_o^* = 3.83$, where b was fixed to the value obtained in vertex model simulations (cf. Fig. 3*D*). (*C*, *Inset*) $\bar{p}$ and Q for individual embryos over time. (*D*) The relationship between the corrected average cell shape index $\bar{p}_{corr}$ and cell shape alignment Q for eight individual wild-type embryos, with each point representing a time point in a single embryo. The cell shape index is corrected by the vertex coordination number z as $\bar{p}_{corr} = \bar{p} - (z - 3)/B$, with $B = 3.85$ (42). Instantaneous cell rearrangement rate per cell in the tissue is represented by the color of each point. The solid line indicates the parameter-free prediction of Eq. **2**. (*D*, *Inset*) Single embryo fit to Eq. **1**. (*E*) p_o^* from single embryo fits to Eq. **1** correlate with the fraction of pentagonal cells f_5, a metric for cell packing disorder in the tissue, at the transition point. The dashed line represents a linear fit to the data. When using a rearrangement-rate cutoff of 0.02 min^{-1} per cell for the single embryo fits, we obtain for this linear fit $p_o^* = 3.755 + 0.27f_5$. (*F*) p_o^* from single-embryo fits to Eq. **1** correlate with the average vertex coordination number, another metric for packing disorder in the tissue, at the transition point. The dashed line represents the previous theoretical prediction for how manyfold vertices influence tissue behavior (42).

cell shapes and cell rearrangement rates. To this end, we investigated how $\bar{p}$ and Q correlate with the instantaneous rate of cell rearrangements occurring within the germband, with higher rearrangement rates associated with more fluid-like behavior and/or larger active driving forces (Fig. 4*C*). The anisotropic vertex model predicts that the solid or fluid behavior of the tissue should depend on both $\bar{p}$ and Q according to Eq. **1**, with only two adjustable parameters, p_o^* and b. We fit Eq. **1** to our experimental data by minimizing a quality-of-fit measure defined as the number of experimental data points on the wrong side of the theoretical transition line, and for simplicity varied only p_o^* while keeping the theoretically determined value for b. Varying the value b leads, at most, to a slight improvement of our fit (*SI Appendix*, Fig. S8). To differentiate between solid-like and fluid-like tissue behavior in the experimental data, we need to choose a cutoff value for the cell rearrangement rate. Choosing a cutoff of 0.02 min^{-1} per cell yielded a best fit with $p_o^* = 3.83$ (solid line, Fig. 4*C*). To confirm that our prediction of a quadratic dependence on Q is supported by the data, we also identified the best fit to a null hypothesis of a Q-independent transition point (horizontal dashed line, Fig. 4*C*). Using our quality-of-fit measure, we found that the Q-dependent fit was always better, independent of the chosen cell rearrangement rate cutoff (*SI Appendix*, Fig. S8).

Comparing the trajectories of individual embryos (Fig. 4 *C*, *Inset*) to the predicted transition in the anisotropic vertex model (Fig. 4*C*), we see that, during early times, when $\bar{p}$ and Q are both increasing, the tissue stays within the predicted solid-like regime. The subsequent rapid decrease in Q brings embryos closer to the transition line. As $\bar{p}$ further increases, individual embryos cross this transition line, which coincides with increased rates of cell rearrangement, at different points $(Q,\bar{p})$. Thus, compared to the isotropic model, the anisotropic vertex model better describes the onset of rapid cell rearrangement and tissue flow during convergent extension with two metrics of cell patterns, $\bar{p}$ and Q, that are both easy to access experimentally.

Accounting for Cell Shape Alignment and Cell Packing Disorder Allows for a Parameter-Free Prediction of Tissue Behavior. While the above results confirm that tissue anisotropy must be taken into account to predict the onset of rapid cell rearrangement, the theoretical prediction in Fig. 4*C* still required a fit parameter p_o^*. Theoretical results suggest that this fit parameter, which is the isotropic transition point in the absence of anisotropic forces, should depend systematically on cell packing disorder quantified by vertex coordination (42) and fraction of pentagonal cells (Fig. 2*D*).

Therefore, we analyzed the $\bar{p}$ and Q data for each embryo individually, by fitting them to Eq. **1** with $b = 0.43$, where we again used p_o^* as the only fit parameter (Fig. 4 *D*, *Inset*). We compared the p_o^* obtained for each embryo (purple point, Fig. 4 *D*, *Inset*) to the average vertex coordination number in the tissue at the time of the transition (green point, Fig. 4 *D*, *Inset*) and found a clear correlation (dashed line, Fig. 4*F*), which fit well with the previous theoretical prediction (42), with no fit parameters.

Combining this previous theoretical prediction of the effects of vertex coordination on the solid–fluid transition in isotropic tissues with our prediction for how cell shape alignment shifts this transition in anisotropic tissues in Eq. **1** generates the following parameter-free prediction of the critical shape index for tissue fluidity:

$$\bar{p}_{crit} = 3.818 + (z-3)/B + 4bQ^2, \qquad [2]$$

where z is the measured average vertex coordination number, and the other parameters are universally determined a priori from vertex model simulations: $B = 3.85$ (42), and $b = 0.43$. To test this prediction, we plot the cell shape index corrected by the vertex coordination number, $\bar{p}_{corr} = \bar{p} - (z-3)/B$, versus cell shape alignment Q in the germband of wild-type embryos and compared it to the theoretical curve given by $\bar{p}_{corr} = 3.818 + 4bQ^2$ (solid line, Fig. 4*D*). Remarkably, this parameter-free prediction described our experimental data well. We compared the quality of fit to alternative parameter-free predictions and found that Eq. **2** consistently provided the best prediction for a wide range of cell rearrangement rate cutoffs (*SI Appendix*, Fig. S8).

Some embryos deviated from the theoretical prediction from ref. 42 (Fig. 4*F*), suggesting that perhaps alternate features of packing disorder may play an important role in those embryos. Thus, we also compared p_o^* obtained from the individual-embryo fits to the respective fraction of pentagons at the time of the transition and found a strikingly clear correlation well described by a linear relation (Fig. 4*E*, dashed line is a linear fit). This relationship quantitatively differs from what we extracted from our vertex model simulations (Fig. 2*D*), indicating again that other aspects of packing disorder may also play a role. Nevertheless, using this linear fit to correct the shape index for each data point by the fraction of pentagonal cells, we obtained an improved prediction of our data (compare Fig. 4*D* to *SI Appendix*, Fig. S9) at the expense of requiring two fit parameters.

Taken together, these results show that we can quantitatively predict the behavior of the germband tissue in wild-type embryos, with no fit parameters using Eq. **2**, from an image of cell patterns in the tissue. To do so, we needed to quantify three observables: cell shapes, cell alignment, and cell packing disorder. We found that vertex coordination and the fraction of pentagonal cells are both good proxies for packing disorder, in vertex model simulations and the germband.

Cell Shape, Alignment, and Tissue Behavior in *snail twist* and *bnt* Mutant Embryos. Since the *Drosophila* germband experiences both internal forces due to myosin planar polarity and external forces from neighboring tissues, we wondered whether our theoretical predictions hold when altering the nature of the forces in the germband. To dissect the effects of internal and external sources of tissue anisotropy, we studied cell patterns in *snail twist* mutant embryos, which lack genes required for invagination of the presumptive mesoderm (57), and in *bcd nos tsl* (*bnt*) mutant embryos, which lack patterning genes required for planar-polarized patterns of myosin localization and axis elongation (22, 47).

First, we analyzed cell shapes and cell shape alignment in the germband of *snail twist* mutant embryos in which the presumptive mesoderm does not invaginate. In *snail twist* embryos, we observed that the germband tissue elongated (Fig. 5*C*) and cell rearrangements occurred (Fig. 5*D*), similar to prior studies (28), although at somewhat reduced rates compared to in wild-type embryos. However, in contrast to wild-type embryos, we found that the cell shape alignment Q was significantly reduced between $t = -5$ min and $t = +8$ min (Fig. 5 *A*, *B*, and *F*), similar to previous reports of other metrics for cell stretching (28). The cell shape index $\bar{p}$ was also reduced during this period (Fig. 5 *A*, *B*, and *E*). These observations are consistent with the idea that external forces from mesoderm invagination produce the transient cell shape elongation and alignment observed in wild-type embryos.

Next, we tested whether our theoretical predictions would describe tissue behavior in *snail twist* embryos, even with their significantly reduced cell alignment. We found that the onset of rapid cell rearrangement in *snail twist* embryos was also well predicted by Eq. **2** (Fig. 5*G*). This was corroborated by comparing the parameters p_o^* of the individual *snail twist* embryo fits to the vertex coordination number at the transition (Fig. 5 *G*, *Inset*), which is close to the previous theoretical prediction (dashed line) (42). Hence, our prediction also held in embryos

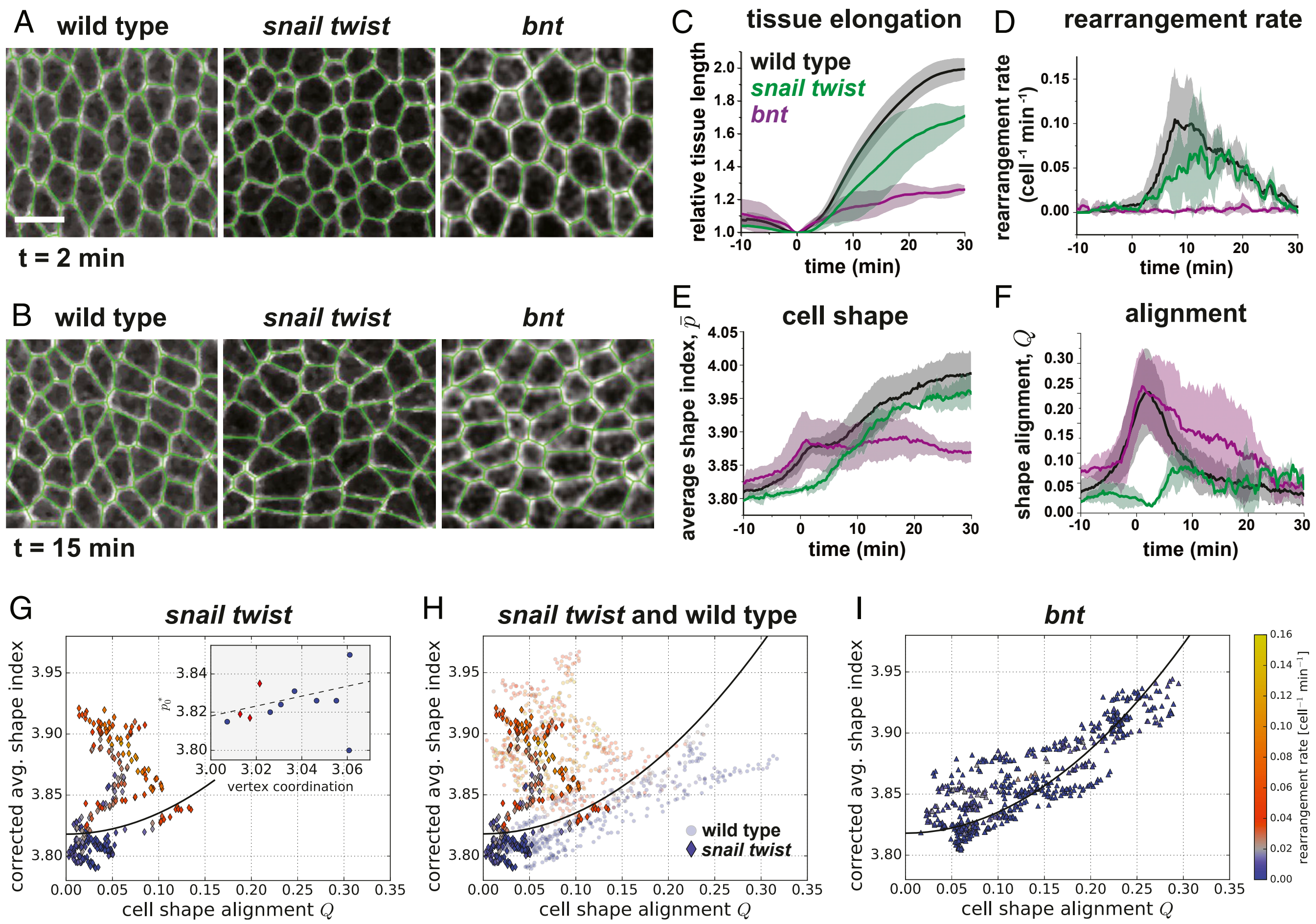

Fig. 5. Cell shape, cell shape alignment, and cell rearrangement rates in the germband of *snail twist* and *bnt* mutant embryos. *snail twist* embryos lack ventral patterning genes required for presumptive mesoderm invagination. *bnt* embryos lack AP patterning genes required for axis elongation and show severely disrupted myosin planar polarity compared to wild type (*SI Appendix*, Fig. S10). (*A* and *B*) Confocal images from time-lapse movies of cell patterns at $t = +2$ min and $t = +15$ min. Cell outlines visualized with fluorescently tagged cell membrane markers: gap43:mCherry in wild type, Spider:GFP in *snail twist*, and Resille:GFP in *bnt*. Polygon representations of cell shapes are overlaid (green). (Scale bar, 10 μm.) (*C*) Tissue elongation is moderately reduced in *snail twist* and severely reduced in *bnt* compared to wild type. (*D*) Cell rearrangement rate is moderately decreased in *snail twist* and severely reduced in *bnt*. (*E*) In *snail twist*, the average cell shape index $\bar{p}$ is reduced compared to in wild type for -5 min $< t < 5$ min. In *bnt*, $\bar{p}$ shows similar behavior to in wild type for $t < 5$ min, but does not show further increases with time for $t > 5$ min. (*F*) In *snail twist*, the cell alignment index Q is strongly reduced for -5 min $< t < 10$ min compared to in wild type. In *bnt*, Q shows similar behavior to in wild type for $t < 5$ min, but relaxes more slowly to low levels. (*C*–*F*) The mean and SD between embryos is plotted (three *snail twist* and five *bnt* embryos with an average of 190 cells per embryo per time point). (*G*–*I*) Relationship between the corrected cell shape index $\bar{p}_{corr}$ and Q for three *snail twist* (*G* and *H*), eight wild-type (*H*), and five *bnt* (*I*) embryos, with each point representing a time point in a single embryo. Instantaneous rearrangement rate is represented by the color of each point. Solid lines represent the prediction of Eq. **2**. (*H*) Tissue behavior in *snail twist* and wild-type embryos, all of which exhibit rapid cell rearrangement during convergent extension, is well described by the prediction of Eq. **2**, which does not require any fitting parameters. Avg., average.

with reduced cell shape alignment Q, where the transition to rapid cell rearrangement occurred at a lower cell shape index $\bar{p}$ compared to in wild-type embryos (Fig. 5*H*).

To investigate how disrupting other forces in the germband affects tissue behavior, we studied cell patterns in *bnt* mutant embryos, which lack AP patterning genes required for axis elongation. These mutant embryos did not display myosin planar polarity, although there was significant myosin present at the apical cortex of cells (*SI Appendix*, Fig. S10). The *bnt* embryos had severe defects in tissue elongation (Fig. 5*C*), cell rearrangement (Fig. 5*D*), and endoderm invagination, but still underwent mesoderm invagination (13, 20, 22, 26, 28, 47). $\bar{p}$ displayed an initial increase (Fig. 5*E*), concomitant with an increase in Q (Fig. 5*F*), similar to in wild-type embryos. After $t =$ 1 min, $\bar{p}$ did not increase further and took on a steady value of 3.87 (Fig. 5*E*). This supports the idea that the further increase in $\bar{p}$ in wild-type embryos is due to internal anisotropies associated with myosin planar polarity or external forces associated with endoderm invagination. Interestingly, Q returned more slowly to low levels in *bnt* compared to wild-type embryos (Fig. 5*F*), suggesting a potential role for myosin planar polarity, cell rearrangements oriented along the AP axis, or endoderm invagination in relaxing cell shape alignment along the DV axis. The *bnt* tissues did not transition to a state of rapid cell rearrangement. This was not consistent with the predictions of Eq. **2** (Fig. 5*I*), which predicts some fluid-like tissue states in the germband of *bnt* embryos, suggesting that either the driving forces are too small or that there are additional barriers that prevent rapid cell rearrangement in these embryos.

Taken together, these findings demonstrate that external forces associated with mesoderm invagination contribute to tissue anisotropy in the germband and that the onset of rapid cell rearrangement can be predicted from cell shape and alignment, even in the absence of forces associated with mesoderm invagination.

Discussion

In this work, we show that cell shape, cell alignment, and packing disorder can be used to understand and predict whether an anisotropic tissue flows and remodels like a fluid or, instead, maintains its shape like a solid. Importantly, in contrast to isotropic tissues, the mechanical behavior of the converging and extending *Drosophila* germband cannot be predicted by cell shape and packing disorder alone. Instead, we show via theoretical analysis and simulation that, in anisotropic tissues, three experimentally accessible metrics—the cell shape index $\bar{p}$, the cell alignment index Q, and packing disorder quantified by either vertex coordination or fraction of pentagonal cells—are required to determine whether an anisotropic tissue flows and remodels or not. We demonstrate that the onset of rapid cell rearrangement in wild-type *Drosophila* embryos is indeed more accurately described by a combination of these three cell-pattern metrics, using an equation with no fit parameters, than by cell shape or packing disorder alone. We further tested this prediction in *snail twist* mutant embryos in which the presumptive mesoderm does not invaginate and found that our parameter-free prediction successfully predicted the onset of rapid cell rearrangement and tissue flow in this case as well. These findings suggest that convergent extension of the *Drosophila* germband might be viewed as a transition to more fluid-like behavior to help accommodate dramatic tissue flows. This raises the possibility that the properties of developing tissues might be tuned to become more fluid-like during rapid morphogenetic events.

A fluid-to-solid jamming transition has recently been reported in mesodermal tissues during zebrafish body axis elongation (8). In contrast to the zebrafish mesoderm in which the transition to more solid-like behavior is associated with an increase in cellular volume fraction (proportion of the tissue occupied by cells), the *Drosophila* germband epithelium comprises tightly packed cells, and its mechanical behavior changes in the absence of any change in cellular volume fraction. Future studies will be needed to explore how the properties of epithelial cells might be regulated during development to tune the mechanical behaviors of the tissues in which they reside.

The vertex model predictions of tissue behavior are independent of the underlying origin of anisotropy, and therefore can be used to predict mechanical behavior of tissues from cell shape patterns, even when external and internal stresses cannot be directly measured. Although our current simulations were not able to access some of the tissue states driven by internal stresses, we found that the cases that were accessible were fully consistent with our simulation results without internal stresses. Importantly, the average cell shape index $\bar{p}$, cell shape alignment index Q, and metrics for packing disorder are easy to access experimentally from snapshots of cell packings in tissues, even in systems where time-lapse live imaging of cell rearrangement and tissue flow is not possible. Thus, this approach may prove useful for studying complex tissue behaviors in a broad range of morphogenetic processes occurring in developing embryos in vivo or organoid systems in vitro.

In our analysis, we characterized the mechanical state of the germband epithelial tissue using the rate of cell rearrangement as the observable. We made this choice because direct measurements of the mechanical properties of the germband remain a significant experimental challenge (6, 7, 14). Generally, higher rates of cell rearrangement could be due to more fluid tissue properties or a stronger driving force, which is the sum of externally applied forces and internally generated mechanical stresses. Based on our Eq. **2** result, the cell shape index and alignment predict the onset of rapid cell rearrangement in the germband. While this would be consistent with the tissue becoming more fluid, it is also possible that the observed increase in cell rearrangement rate is, at least in part, due to an increase in the driving force while the tissue remains solid.

To parse this possibility further, it is useful to consider a solid tissue, where the tissue will flow only if it is pulled with a force above some threshold called the yield stress. If the tissue is deeply in the solid state, far from the solid–fluid transition, and the applied force is far above the yield stress, one would expect cells to acquire elongated shapes and transiently form manyfold vertices during cell rearrangements in response to the applied force. The rearrangement rate would correlate with the cell shape index, after accounting for packing disorder and alignment, which is similar to what we predict with our fluid–solid model. However, based on our vertex model simulations, we would not expect to see tissue states with high shape index $\bar{p}$ and low alignment Q associated with high rearrangement rates for solid tissues. Since we do observe such tissue behavior during germband extension, this suggests that the germband is more fluid-like during these periods with high cell rearrangement rates.

Of course, it could be that the tissue is a very weak yield-stress solid, so that it becomes fluid-like under very small applied forces. This is consistent with the observations that the large majority of rearrangements are oriented along the head-to-tail body axis (21, 22, 46, 47, 58), and the time period of rapid cell rearrangement (Fig. 1*C*) coincides with the period of planar-polarized myosin (13, 25, 46). Direct mechanical measurements of the germband have not been conducted during axis elongation, but ferrofluid droplet and magnetic-bead microrheology measurements have probed the mechanical behavior of the epithelium prior to germband extension in the cellularizing embryo. These studies report that tissue behavior is predominantly elastic (solid-like) over timescales less than several minutes and suggest fluid-like behavior on the longer, ~30-min timescales relevant for germband extension (51, 52). These measurements might also be consistent with a weak yield-stress solid, an interpretation that would be supported by the near absence of cell rearrangements prior to germband extension. Taken together, these observations suggest that, over the time period that we describe the germband as “fluid-like,” it could actually be a very weak yield-stress solid.

Though there is often little functional difference between a fluid and weak yield-stress solid, the difference may be relevant for mutant *bnt* embryos, whose behavior is not well captured by our theoretical predictions. In particular, we observed *bnt* tissues with $\bar{p}$, Q, and cell packing disorder that would be predicted to display fluid-like behavior, but did not undergo rapid cell rearrangement. This suggests that in these embryos, the driving forces are not sufficient to overcome the yield stress. One obvious explanation for this is that the germband in *bnt* embryos experiences altered forces associated with disrupted myosin planar polarity (22) and defects in endoderm invagination, which would contribute to a reduced driving force. Alternatively, additional barriers to cell rearrangement in *bnt* mutants, of the sort described in ref. 59, could also explain this behavior.

Similarly, our vertex model does not predict the observed decrease in cell rearrangement rates after 20 min of axis elongation (Fig. 1*C*). Given the observed high values of $\bar{p}$ and low values of Q, our model would still predict fluid-like behavior. Just as in the *bnt* mutants, this discrepancy could be explained by a decreased driving force or additional barriers to cell rearrangement. The former explanation is supported by the observation that myosin planar polarity reaches a maximum 5 to 10 min after the onset of axis elongation and then decreases during the rest of the process (25, 28, 46), while the latter could potentially be explained by maturation of cell junctions or changes to adhesive interactions over the course of embryonic development (60, 61).

Consistent with the notion of additional barriers to cell rearrangement, recent work suggests that local remodeling of active junctional tension at cell–cell contacts only occurs above a critical strain threshold in cultured epithelial cells (59, 62). This is consistent with a growing body of work that points toward important roles for membrane trafficking and E-cadherin turnover in junctional remodeling during *Drosophila* epithelial morphogenesis (11, 63–65). Indeed, such a mechanism of mechanosensitive barriers to junctional remodeling and cell rearrangement can be added to standard vertex models to explain such weak yield-stress behavior (59).

Moving forward, it will be interesting to explore experimentally how the nature of internal and external forces contribute to tissue mechanics, cell rearrangement, and tissue flows in the germband and other developing epithelial tissues. Incorporating these features into more sophisticated vertex models will contribute to understanding the diverse behaviors of living tissues, and the approaches we develop here will be useful for interrogating these questions.

Methods

Embryos were generated at 23 °C and analyzed at room temperature. Cell outlines were visualized with gap43:mCherry (53), Spider:GFP, or Resille:GFP cell-membrane markers. Embryos were imaged on a Zeiss LSM880 laser-scanning confocal microscope. Time-lapse movies were analyzed with SEGGA software in MATLAB (28) for quantifying cell shapes and cell rearrangement rates, PIVlab (Version 1.41) in MATLAB (66) for quantifying tissue elongation, and custom code for quantifying cell alignment using the triangle method (55, 56, 67). The vertex model describes an epithelial tissue as a planar tiling of N cellular polygons, where the degrees of freedom are the vertex positions (33). Forces in the model were defined such that cell perimeters and areas act as effective springs with a preferred perimeter p_0 and a preferred area of one, which is implemented via an effective energy functional (45). Unless otherwise noted, error bars are the SD. The data that support the findings of this study are included in the paper and *SI Appendix*. The custom code used in this study to extract the average triangle-based Q tensor from images segmented using SEGGA (28) is available at https://github.com/mmerkel/triangles-segga. Details can be found in *SI Appendix, SI Materials and Methods*.

ACKNOWLEDGMENTS. We thank Erik Boyle for assistance with data processing; Dene Farrell and Jennifer Zallen for the use of SEGGA, a segmentation and quantitative image analysis toolset; Adam Martin for the sqh-gap43:mCherry fly stock; and the Bloomington Drosophila Stock Center for fly stocks. We thank an anonymous reviewer of our manuscript for suggesting that we develop a more quantitative analysis of packing disorder for our data, ultimately resulting in a significant improvement in our ability to predict tissue flow. This work was supported by NSF Civil, Mechanical, and Manufacturing Innovation Grant 1751841 (to K.E.K.); NSF Grants DMR-1352184 and POLS-1607416 (to M.L.M.); and NSF Research Experiences for Undergraduates Grant DMR-1460784 (to L.B.S.). M.L.M., M.M., and G.E.-T. were supported by Simons Grants 446222 and 454947; and NIH Grant R01GM117598. K.E.K. holds a Burroughs Wellcome Fund Career Award at the Scientific Interface, Clare Boothe Luce Professorship, and Packard Fellowship.

1. R. Keller, Developmental biology. Physical biology returns to morphogenesis. *Science* **338**, 201–203 (2012).
2. D. Gilmour, M. Rembold, M. Leptin, From morphogen to morphogenesis and back. *Nature* **541**, 311–320 (2017).
3. J. Zhou, H. Y. Kim, L. A. Davidson, Actomyosin stiffens the vertebrate embryo during crucial stages of elongation and neural tube closure. *Development* **136**, 677–688 (2009).
4. L. A. Davidson, Embryo mechanics: Balancing force production with elastic resistance during morphogenesis. *Curr. Top. Dev. Biol.* **95**, 215–241 (2011).
5. O. Campàs *et al*., Quantifying cell-generated mechanical forces within living embryonic tissues. *Nat. Methods* **11**, 183–189 (2014).
6. R. M. Herrera-Perez, K. E. Kasza, Biophysical control of the cell rearrangements and cell shape changes that build epithelial tissues. *Curr. Opin. Genet. Dev.* **51**, 88–95 (2018).
7. G. A. Stooke-Vaughan, O. Campàs, Physical control of tissue morphogenesis across scales. *Curr. Opin. Genet. Dev.* **51**, 111–119 (2018).
8. A. Mongera *et al*., A fluid-to-solid jamming transition underlies vertebrate body axis elongation. *Nature* **561**, 401–405 (2018).
9. A. K. Lawton *et al*., Regulated tissue fluidity steers zebrafish body elongation. *Development* **140**, 573–582 (2013).
10. R. J. Tetley *et al*., Tissue fluidity promotes epithelial wound healing. *Nat. Phys.* **15**, 1195–1203 (2019).
11. K. V. Iyer, R. Piscitello-Gómez, J. Paijmans, F. Jülicher, S. Eaton, Epithelial viscoelasticity is regulated by mechanosensitive E-cadherin turnover. *Curr. Biol.* **29**, 578–591.e5 (2019).
12. M. Dicko *et al*., Geometry can provide long-range mechanical guidance for embryogenesis. *PLOS Comput. Biol.* **13**, e1005443 (2017).
13. S. J. Streichan, M. F. Lefebvre, N. Noll, E. F. Wieschaus, B. I. Shraiman, Global morphogenetic flow is accurately predicted by the spatial distribution of myosin motors. *eLife* **7**, e27454 (2018).
14. O. Campàs, A toolbox to explore the mechanics of living embryonic tissues. *Semin. Cell Dev. Biol.* **55**, 119–130 (2016).
15. E. Walck-Shannon, J. Hardin, Cell intercalation from top to bottom. *Nat. Rev. Mol. Cell Biol.* **15**, 34–48 (2014).
16. A. Vichas, J. A. Zallen, Translating cell polarity into tissue elongation. *Semin. Cell Dev. Biol.* **22**, 858–864 (2011).
17. M. T. Butler, J. B. Wallingford, Planar cell polarity in development and disease. *Nat. Rev. Mol. Cell Biol.* **18**, 375–388 (2017).
18. M. Simons, M. Mlodzik, Planar cell polarity signaling: From fly development to human disease. *Annu. Rev. Genet.* **42**, 517–540 (2008).
19. R. Hale, D. Strutt, Conservation of planar polarity pathway function across the animal kingdom. *Annu. Rev. Genet.* **49**, 529–551 (2015).
20. J. A. Zallen, E. Wieschaus, Patterned gene expression directs bipolar planar polarity in *Drosophila*. *Dev. Cell* **6**, 343–355 (2004).
21. C. Bertet, L. Sulak, T. Lecuit, Myosin-dependent junction remodelling controls planar cell intercalation and axis elongation. *Nature* **429**, 667–671 (2004).
22. J. T. Blankenship, S. T. Backovic, J. S. Sanny, O. Weitz, J. A. Zallen, Multicellular rosette formation links planar cell polarity to tissue morphogenesis. *Dev. Cell* **11**, 459–470 (2006).
23. M. Rauzi, P. Verant, T. Lecuit, P.-F. Lenne, Nature and anisotropy of cortical forces orienting *Drosophila* tissue morphogenesis. *Nat. Cell Biol.* **10**, 1401–1410 (2008).
24. R. Fernandez-Gonzalez, S. M. Simões, J. C. Röper, S. Eaton, J. A. Zallen, Myosin II dynamics are regulated by tension in intercalating cells. *Dev. Cell* **17**, 736–743 (2009).
25. R. J. Tetley, G. B. Blanchard, A. G. Fletcher, R. J. Adams, B. Sanson, Unipolar distributions of junctional Myosin II identify cell stripe boundaries that drive cell intercalation throughout *Drosophila* axis extension. *eLife* **5**, e12094 (2016).
26. L. C. Butler *et al*., Cell shape changes indicate a role for extrinsic tensile forces in *Drosophila* germ-band extension. *Nat. Cell Biol.* **11**, 859–864 (2009).
27. C. M. Lye *et al*., Mechanical coupling between endoderm invagination and axis extension in *Drosophila*. *PLoS Biol.* **13**, e1002292 (2015).
28. D. L. Farrell, O. Weitz, M. O. Magnasco, J. A. Zallen, SEGGA: A toolset for rapid automated analysis of epithelial cell polarity and dynamics. *Development* **144**, 1725–1734 (2017).
29. M. Rauzi *et al*., Embryo-scale tissue mechanics during *Drosophila* gastrulation movements. *Nat. Commun.* **6**, 8677 (2015).
30. A. G. Fletcher, M. Osterfield, R. E. Baker, S. Y. Shvartsman, Vertex models of epithelial morphogenesis. *Biophys. J.* **106**, 2291–2304 (2014).
31. S. Alt, P. Ganguly, G. Salbreux, Vertex models: From cell mechanics to tissue morphogenesis. *Philos. Trans. R. Soc B Biol. Sci.* **372**, 20150520 (2017).
32. T. Nagai, H. Honda, A dynamic cell model for the formation of epithelial tissues. *Philos Mag Part B* **81**, 699–719 (2001).
33. R. Farhadifar, J. C. Röper, B. Aigouy, S. Eaton, F. Jülicher, The influence of cell mechanics, cell-cell interactions, and proliferation on epithelial packing. *Curr. Biol.* **17**, 2095–2104 (2007).
34. M. A. Spencer, J. Lopez-Gay, H. Nunley, Y. Bellaïche, D. K. Lubensky, Multicellular actomyosin cables in epithelia under external anisotropic stress. arXiv:1809.04569 (12 September 2018).
35. D. B. Staple *et al*., Mechanics and remodelling of cell packings in epithelia. *Eur. Phys. J. E Soft Matter* **33**, 117–127 (2010).
36. B. Aigouy *et al*., Cell flow reorients the axis of planar polarity in the wing epithelium of *Drosophila*. *Cell* **142**, 773–786 (2010).
37. M. Krajnc, S. Dasgupta, P. Ziherl, J. Prost, Fluidization of epithelial sheets by active cell rearrangements. *Phys. Rev. E* **98**, 22409 (2018).
38. D. Bi, J. H. Lopez, J. M. Schwarz, M. L. Manning, Energy barriers and cell migration in densely packed tissues. *Soft Matter* **10**, 1885–1890 (2014).
39. D. Bi, J. H. Lopez, J. M. Schwarz, M. L. Manning, A density-independent rigidity transition in biological tissues. *Nat. Phys.* **11**, 1074–1079 (2015).
40. D. Bi, X. Yang, M. C. Marchetti, M. L. Manning, Motility-driven glass and jamming transitions in biological tissues. *Phys. Rev. X* **6**, 21011 (2016).
41. J.-A. Park *et al*., Unjamming and cell shape in the asthmatic airway epithelium. *Nat. Mater.* **14**, 1040–1048 (2015).
42. L. Yan, D. Bi, Multicellular rosettes drive fluid-solid transition in epithelial tissues. *Phys. Rev. X* **9**, 11029 (2019).
43. D. M. Sussman, M. Merkel, No unjamming transition in a Voronoi model of biological tissue. *Soft Matter* **14**, 3397–3403 (2018).
44. M. Merkel, M. L. Manning, A geometrically controlled rigidity transition in a model for confluent 3D tissues. *New J. Phys.* **20**, 22002 (2018).
45. M. Merkel, K. Baumgarten, B. P. Tighe, M. L. Manning, A minimal-length approach unifies rigidity in underconstrained materials. *Proc. Natl. Acad. Sci. U.S.A.* **116**, 6560–6568 (2019).
46. K. E. Kasza, D. L. Farrell, J. A. Zallen, Spatiotemporal control of epithelial remodeling by regulated myosin phosphorylation. *Proc. Natl. Acad. Sci. U.S.A.* **111**, 11732–11737 (2014).

47. K. D. Irvine, E. Wieschaus, Cell intercalation during *Drosophila* germband extension and its regulation by pair-rule segmentation genes. *Development* **120**, 827–841 (1994).
48. C. Collinet, M. Rauzi, P.-F. Lenne, T. Lecuit, Local and tissue-scale forces drive oriented junction growth during tissue extension. *Nat. Cell Biol.* **17**, 1247–1258 (2015).
49. J. C. Yu, R. Fernandez-Gonzalez, Local mechanical forces promote polarized junctional assembly and axis elongation in *Drosophila*. *eLife* **5**, 10757 (2016).
50. F. Serwane *et al*., In vivo quantification of spatially varying mechanical properties in developing tissues. *Nat. Methods* **14**, 181–186 (2017).
51. K. Doubrovinski, M. Swan, O. Polyakov, E. F. Wieschaus, Measurement of cortical elasticity in *Drosophila melanogaster* embryos using ferrofluids. *Proc. Natl. Acad. Sci. U.S.A.* **114**, 1051–1056 (2017).
52. A. D'Angelo, K. Dierkes, C. Carolis, G. Salbreux, J. Solon, In vivo force application reveals a fast tissue softening and external friction increase during early embryogenesis. *Curr. Biol.* **29**, 1564–1571.e6 (2019).
53. A. C. Martin, M. Gelbart, R. Fernandez-Gonzalez, M. Kaschube, E. F. Wieschaus, Integration of contractile forces during tissue invagination. *J. Cell Biol.* **188**, 735–749 (2010).
54. J. A. Zallen, R. Zallen, Cell-pattern disordering during convergent extension in *Drosophila*. *J. Phys. Condens. Matter* **16**, S5073–S5080 (2004).
55. R. Etournay *et al*., Interplay of cell dynamics and epithelial tension during morphogenesis of the *Drosophila* pupal wing. *eLife* **4**, e07090 (2015).
56. M. Merkel *et al*., Triangles bridge the scales: Quantifying cellular contributions to tissue deformation. *Phys. Rev. E* **95**, 32401 (2017).
57. M. Leptin, B. Grunewald, Cell shape changes during gastrulation in *Drosophila*. *Development* **110**, 73–84 (1990).
58. A. C. Paré *et al*., A positional Toll receptor code directs convergent extension in *Drosophila*. *Nature* **515**, 523–527 (2014).
59. M. F. Staddon, K. E. Cavanaugh, E. M. Munro, M. L. Gardel, S. Banerjee, Mechanosensitive junction remodeling promotes robust epithelial morphogenesis. *Biophys. J.* **117**, 1739–1750 (2019).
60. T. J. C. Harris, Adherens junction assembly and function in the *Drosophila* embryo. *Int. Rev. Cell Mol. Biol.* **293**, 45–83 (2012).
61. Z. Sun, Y. Toyama, Three-dimensional forces beyond actomyosin contraction: Lessons from fly epithelial deformation. *Curr. Opin. Genet. Dev.* **51**, 96–102 (2018).
62. K. E. Cavanaugh, M. F. Staddon, E. Munro, S. Banerjee, M. L. Gardel, RhoA mediates epithelial cell shape changes via mechanosensitive endocytosis. *Dev. Cell* **52**, 152–166.e5 (2020).
63. C. E. Jewett *et al*., Planar polarized Rab35 functions as an oscillatory ratchet during cell intercalation in the *Drosophila* epithelium. *Nat. Commun.* **8**, 476 (2017).
64. A. Sumi *et al*., Adherens junction length during tissue contraction is controlled by the mechanosensitive activity of actomyosin and junctional recycling. *Dev. Cell* **47**, 453–463.e3 (2018).
65. G. R. Kale *et al*., Distinct contributions of tensile and shear stress on E-cadherin levels during morphogenesis. *Nat. Commun.* **9**, 5021 (2018).
66. W. Thielicke, E. J. Stamhuis, PIVlab—towards user-friendly, affordable and accurate digital particle image velocimetry in MATLAB. *J. Open Res. Softw.* **2**, e30 (2014).
67. R. Etournay *et al*., TissueMiner: A multiscale analysis toolkit to quantify how cellular processes create tissue dynamics. *eLife* **5**, e14334 (2016).